Check for updates

Thermally driven *in situ* exsolution of Ni nanoparticles from (Ni, Gd)CeO$_2$ for high-performance solid oxide fuel cells†

Jeiwan Tan,[a] Daehee Lee, [iD][a] Jihoon Ahn, [iD][a] Bokyung Kim,[a] Joosun Kim[b] and Jooho Moon [iD]*[a]

In situ exsolution of metal nanoparticles affords a high content and uniform distribution of metal nanocatalysts without complex synthetic processes. To implement this strategy in practical electrodes for solid oxide fuel cells, understanding the exsolution process in terms of synthesis temperature and atmosphere is a prerequisite. Herein, we demonstrate that Ni:Gd co-doped ceria (GNDC) can be effectively used as an *in situ* exsolution system, from which substitutionally doped Ni is thermally exsolved as NiO nanoparticles strongly attached to the surface of GNDC, the host oxide, and subsequently reduced to a Ni nanocatalyst under anodic operation conditions. The exsolution procedures were characterized by X-ray diffraction, Raman spectroscopy, and transmission electron spectroscopy, which revealed that the evolution of Ni nanoparticles could be solely controlled by thermal treatment. The thermally exsolved Ni nanocatalyst from the 5 mol% Ni-doped GNDC electrode exhibits a polarization resistance comparable to that of the mechanically mixed Ni-GDC composite electrode, with a significant increase in the calculated triple phase boundary density despite having a low Ni volume fraction. By employing the GNDC layer as a functional layer of an anode-supported SOFC, we demonstrated the utilization of the thermally exsolved Ni nanocatalyst combined with fluorite-structured doped-ceria as an electrode of SOFCs at low temperature.

Introduction

In situ exsolution of metal nanoparticles has been employed as a promising strategy to obtain nano-electrocatalysts for electrochemical energy converters such as fuel cells and electrolysers.[1–4] In this approach, a catalytically active metallic element is initially dissolved in an oxide host and subsequently exsolved from the lattice by reduction, thermal treatment, or applying an electrochemical potential.[4–6] Perovskite oxide (ABO$_3$) materials are most frequently studied for this phenomenon, in which catalytically active metal ions are doped into the B-site, which subsequently evolve as metal nanoparticles. The generated metal nanoparticles (such as Ni, Co, Mn, Fe, Ag, Ru, *etc.*) exhibit a diameter of 10–20 nm with a high surface-to-volume ratio, and thus possess a high active-site density.[2,7–11] Furthermore, the evolved nanoparticles exhibit not only a uniform distribution

owing to their inherent homogeneity in the host oxide, but also an anchored structure strongly bound to the parent oxide, thus preventing agglomeration-driven deactivation.[12,13] However, the exsolution process for perovskite oxides requires an additional treatment, in which the host oxide needs to be exposed to a reducing atmosphere for up to 10 h at elevated temperatures (>800 °C).[3,6,13–15] For a facile exsolution process, application of an electrochemical potential has been demonstrated to assist the reduction of metal nanoparticles; however, a thermal treatment at high temperatures (900 °C) was still necessary for the electrochemically driven exsolution.[6] In addition, perovskite oxide electrodes are rarely employed along with state-of-the-art fluorite-structured electrolytes because of chemical instability. For example, interdiffusion of metal ions at the electrode/ electrolyte interface leads to the formation of unnecessary and undesirable phases.[16] In this regard, a simple and efficient exsolution process using oxide hosts chemically suitable for fluorite-structured electrolytes is important for *in situ* exsolved nanocatalyst systems.

Electrodes for solid oxide fuel cells (SOFCs) should possess not only a high catalytic activity for the electrochemical reaction, but also conduction pathways for both electrons and ions to maximize the active sites, *i.e.*, triple phase boundary (TPB) density.[17,18] From this perspective, composite electrodes consisting of a metallic catalyst and an ionic conductor have been

[a]*Department of Materials Science and Engineering, Yonsei University, 50 Yonsei-ro, Seodaemun-gu, Seoul 03722, Republic of Korea. E-mail: jmoon@yonsei.ac.kr*

[b]*High-Temperature Energy Materials Research Center, Korea Institute of Science and Technology, Seoul 02792, Republic of Korea*

† Electronic supplementary information (ESI) available: Calculated lattice parameter of GNDC, Raman spectroscopy of GDC powder, scattering intensities of the lattice fringe of HR-TEM, image analysis to estimate TPB density created by the Ni nanocatalyst, additional SEM image, IV characteristics, and EIS data. See DOI: 10.1039/c8ta05978k

commonly used.[19–21] The ionic conductor can also play a role in alleviating the mechanical stress caused by the thermal expansion coefficient (TEC) mismatch between the solid oxide electrolyte and the electrode. On the other hand, the desirable electrode structure can be accomplished by using a mixed ionic and electronic conductor (MIEC) as a host oxide on which isolated metal nanoparticles are exsolved as a catalyst, leading to a maximum TPB density. In this regard, perovskite or rutile oxides such as $Sr_2FeMo_{0.65}Ni_{0.35}O_{6-\delta}$,[5] $Sr_{0.95}(Ti_{0.3}Fe_{0.63}Ni_{0.07})O_{3-\delta}$,[10] $(La_{0.75}Sr_{0.25})(Cr_{0.5}Mn_{0.5-x}Ni_x)O_{3-\delta}$,[22] $(La_{0.2}Sr_{0.8})(Ti_{1-x}Ni_x)O_{3-\delta}$,[23] and $NbTi_{0.5}Ni_{0.5}O_4$ (ref. 3 and 24) have been employed as host oxides for the *in situ* exsolved electrodes. However, perovskite or rutile-based MIECs are thermally instable compared to fluorite-structured electrolytes, which could restrict the long-term stability of the devices.[24,25]

Fluorite-structured doped ceria has been widely used as a solid oxide electrolyte at low temperatures (<650 °C). Doped ceria can exhibit MIEC properties when reduced while maintaining mechanical compatibility with the electrolyte, which renders it a promising host oxide in the composite electrode.[26,27] Recently, Pilger *et al.* demonstrated that Pt nanocatalysts can be generated from the initially doped ceria host by heat treatment at above 900 °C under ambient air.[28] It was also demonstrated that Ni can be initially doped into ceria and subsequently exsolved as a nanocatalyst. Qi *et al.* employed single-phase $Ce_{0.85}Ni_{0.15}O_2$ as a cathode in a solid oxide electrolysis cell for direct carbon dioxide electrolysis. Although the Ni-exsolved electrode showed improved electrocatalytic properties, Ni exsolution required high-temperature reduction at 1000 °C for 3 h.[29] $Ce_{0.9}Ni_{0.1}O_2$ has been used as an anode of a SOFC; however, its electrode performance was inferior to that of a conventional composite anode (*i.e.*, Ni + doped ceria), mainly due to insufficient ionic conductivity of the CeO_2 host (evolved after Ni exsolution).[30] Moreover, there is no in-depth understanding of Ni exsolution from fluorite-structured ceria, which makes it difficult to control the catalytic activity of Ni nanocatalysts.

Herein, we present thermally driven *in situ* exsolution of a Ni nanocatalyst using gadolinium-doped ceria ($Gd_xCe_{1-x}O_{2-\delta}$, GDC) as an oxide host. Ni:Gd co-doped ceria ($Gd_{2-x}Ni_xCe_{0.8}O_{2-\delta}$, GNDC) was synthesized to form substitutionally doped Ni into the GDC host. The sintering of GNDC particles induced the exsolution of NiO nanoparticles on the surface of GDC, which was subsequently reduced to a Ni nanocatalyst anchored on the GDC grains under a reducing atmosphere. To evaluate the electrode performance, electrochemical impedance spectroscopy (EIS) was employed to characterize the GNDC symmetrical electrode as well as the mechanically mixed Ni-GDC composite electrode for comparison under reducing operation conditions. The polarization resistance (R_p), particularly associated with the electrochemical charge-transfer reaction, of the GNDC electrode was smaller than that of the Ni-GDC composite electrode owing to the high TPB density afforded by the exsolved Ni nanocatalyst. The unique anchored structure of the Ni nanocatalyst onto GDC imparted thermal and electrochemical stabilities under harsh operation conditions. Furthermore, GNDC was employed as an anode functional layer of a SOFC and showed

comparable current density with respect to that of the mechanically mixed Ni-GDC composite counterpart, despite only ~2 vol% of Ni catalyst.

Results and discussion

Characterization of exsolution from GNDCs

GNDC powders capable of *in situ* exsolution of the Ni nanocatalyst were prepared by a Pechini-type sol–gel synthesis. Details of the synthesis process are described in the Experimental section. Fig. 1a shows the X-ray diffraction (XRD) profiles of the as-prepared GNDC powders calcined at 600 °C with five different Ni contents ($Gd_{0.2-x}Ni_xCe_{0.8}O_{2-\delta}$; $x = 0.01$, 0.03, 0.05, 0.07, and 0.09). The total moles of the dopants, *i.e.*, the moles of (Ni + Gd), were kept at 0.2, and each sample was denoted by its Ni content as GNDCx (x mol%). For comparison, the XRD profile of the synthesized GDC with the same doping level (*i.e.*, $Gd_{0.2}Ce_{0.8}O_{2-\delta}$, denoted as GDC20) was also obtained. Strong diffraction of cubic fluorite (JCPDS 75-0161) was observed for all the samples, implying that incorporation of Ni did not significantly alter the crystal structure of GDC. On the other hand, NiO diffractions (JCPDS 78-0643) were undetectable in all the samples. This can be explained by two hypotheses: (i) Ni is doped into either the substitutional site or the interstitial site of the GDC lattice[31,32] and (ii) the crystalline size of undoped or composited NiO might be too small to be detected by XRD. As shown in Fig. 1b, the (311) diffraction peak arising from GNDC gradually shifted toward higher angles with increasing Ni content in GNDC up to 5 mol%, while Ni addition over 5 mol%
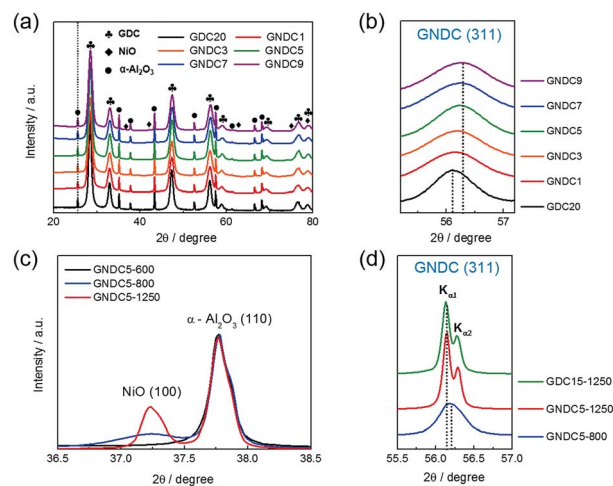

Fig. 1 (a) XRD patterns of GDC20 and five different compositions of GNDC with various Ni doping ratios calcined at 600 °C. There are no detectable NiO peaks regardless of the Ni doping ratio. (b) Enlarged GNDC (311) peaks shift toward high angles as the Ni doping ratio increases up to 5 mol% and its position is almost unchanged over 5 mol%. (c) Magnified NiO (100) peaks for the GNDC5 sample at various annealing temperatures. The NiO peak appears at 800 °C and further crystallizes at 1250 °C. (d) Enlarged GNDC (311) peaks of GNDC5-800 and GNDC5-1250 are compared with that of GDC15-1250. The position of the GNDC (311) peak shifts toward lower angles after annealing at 1250 °C, which coincides with that of GDC15-1250.

caused nearly no further change in the peak position. This observation suggests that the substitutionally doped Ni induces lattice distortion because its ionic radius is smaller than that of the Ce host (Ni^{2+} = 0.69 Å, Ce^{4+} = 0.97 Å), obeying Vegard's law for a solid solution.[30] According to a previous study on the interstitial doping of Ni into CeO_2,[31] the lattice constant of CeO_2 (calcined at 450 °C) decreased up to 4 mol% Ni-doping due to the substitutional replacement of Ce by Ni ions, but increased above 4 mol% Ni-doping due to interstitial incorporation. In contrast, we observed the reduction of the lattice constant only up to 5 mol% of Ni doping, possibly indicating that the interstitial doping is suppressed when calcined at 600 °C. For a precise assessment, the lattice parameters of the GNDC samples as a function of Ni content were calculated from the XRD results by the reference intensity ratio method, as presented in Fig. S1.†[33] The lattice parameters of GNDCs linearly decreased upon the addition of 1–5 mol% Ni, while they became nearly invariant over 5 mol%. It should be noted that the increased Ni content in GNDC accompanies a decrease in the Gd content, which might concurrently cause the observed lattice shrinkage. We observed lattice shrinkage of GNDCs when Ni was doped at 1–5 mol% corresponding to a Gd content variation of 19–15 mol%. However, previous studies showed that the lattice parameter of GDC gradually shrinks as the Gd content decreases from 20 to 10 mol%.[34,35] In this regard, it can be inferred that the Ni content, rather than the Gd content, predominantly determines the lattice constant of GNDC.

Fig. 1c shows the XRD profiles of NiO (100) for the GNDC5 samples as a function of air-annealing temperature. To precisely evaluate the XRD peak variation, we employed an internal standard method by intentionally mixing α-Al_2O_3 powder with the samples. While the NiO (100) peak was not detectable when the samples were annealed at 600 °C (denoted as GNDC5-600), it appeared at 800 °C (GNDC5-800) and was clearly observed after annealing at 1250 °C (GNDC5-1250). The evolution of NiO upon air annealing above 800 °C entailed the recovery of the GNDC (311) peak position, as revealed in Fig. 1d. The GNDC (311) peak shifted toward lower angles upon annealing at 1250 °C and coincided with the peak for 15 mol% GDC annealed at 1250 °C (denoted as GDC15-1250). The identical peak position of GNDC5-1250 and GDC15-1250 possibly indicated that the dopant level of GNDC5-1250 is the same as that of GDC15-1250. In other words, all Ni ions are exsolved from GNDC5 upon annealing at 1250 °C. Note that 5 mol% NiO content is sufficient for detection by XRD, as observed for the air-annealed samples over 800 °C, while NiO particles are able to grow rapidly upon annealing over 500 °C.[36] If Ni existed as a separate phase with GNDC5 without being doped, the NiO phase would have been observable by XRD after air annealing at 600 °C. Therefore, it is hypothesized that Ni is successfully incorporated into the vacant sites of Ce, forming a solid solution of GNDC5 with the maximum solubility at 5 mol%. Upon subsequent air annealing at 800–1250 °C, Ni is exsolved from the lattice to form the NiO phase.

To verify this hypothesis, the vibrational properties of GNDC5 as a function of air-annealing temperature were studied by Raman spectroscopy, as shown in Fig. 2. The most intense
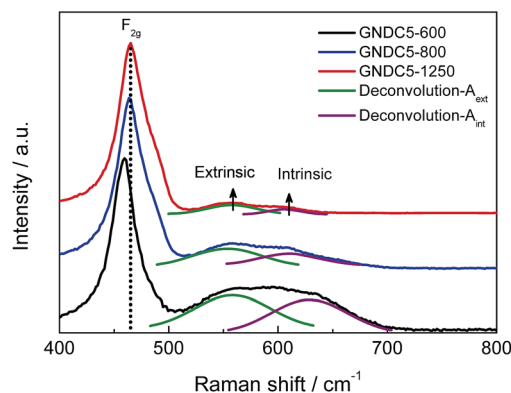

Fig. 2 Raman spectra of GNDC5 powders annealed at 600, 800, and 1250 °C. F_{2g} mode corresponds to the symmetric vibration of oxygen ions around Ce^{4+}, which blue-shifts with increasing annealing temperature. Broad features in the 500–650 cm^{-1} region represent oxygen vacancies, which could be deconvoluted into extrinsic and intrinsic oxygen vacancies.

peak near 460 cm^{-1} indicated the F_{2g} mode of a cubic fluorite-structured ceria (space group $Fm3m$), which originated from the symmetrical stretching of oxygen ions around the Ce cations.[29,37–41] On the other hand, the broad features in the 500–650 cm^{-1} region were ascribed to the non-degenerate Raman-inactive mode of the oxygen vacancies.[37,38] These vibrational modes were strongly associated with substitutional doping of the Ce cations, which gave rise to a red-shifted F_{2g} peak as well as an enhanced non-degenerate mode of oxygen vacancies owing to the increased concentration of oxygen vacancies by doping.[38,39] If Ni is located at the Ce lattice site within the maximum solubility of 5 mol% as hypothesized, 1 mole of Ni doping would generate 1 mole of oxygen vacancies to conserve charge neutrality, according to the Kröger–Vink notation:

$$NiO \xrightarrow{CeO_2} Ni''_{Ce} + O_O^\times + V_O^{\cdot\cdot} \tag{1}$$
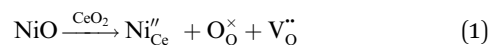
The oxygen vacancy generated upon 1 mole of Ni doping is twice that formed upon 1 mole of Gd doping; thus, the vibration modes in Raman spectra would drastically vary depending on the valence state of Ni if Ni is initially substitutionally doped into GNDC5-600. The F_{2g} peak blue-shifted gradually as the air-annealing temperature of GNDC5 increased, accompanying the diminished non-degenerate mode as plotted in Fig. 2. The non-degenerate mode can be deconvoluted into two sub-peaks: the one at ~560 cm^{-1} was assigned to oxygen vacancies generated upon the replacement of Ce with the dopant, while the other at ~610 cm^{-1} was ascribed to the intrinsic oxygen vacancies owing to the nonstoichiometry of ceria.[38,41] Typically, the ratio of the integrated peak area of the non-degenerate mode to that of the main peak (F_{2g}) reflects the relative amount of oxygen vacancies in the samples.[42] For GNDC5 annealed at different temperatures, the peak area (A) of the deconvoluted non-degenerate mode and F_{2g} mode peaks was obtained after normalization based on the F_{2g} peak intensity. $A_{F_{2g}}$, A_{ext}, and A_{int} denote the peak area of the F_{2g} peak, the extrinsic oxygen vacancy peak at ~560 cm^{-1}, and the intrinsic oxygen vacancy peak at

This journal is © The Royal Society of Chemistry 2018

J. Mater. Chem. A, 2018, **6**, 18133–18142 | **18135**

~610 cm^{-1}, respectively. The area ratio representing the relative amount of extrinsic oxygen vacancies was defined as R_{ext} ($= A_{ext}/A_{F_{2g}}$), whereas R_{int} ($= A_{int}/A_{F_{2g}}$) corresponded to the relative amount of intrinsic oxygen vacancies. As shown in Fig. S2a,† significant decreases in both R_{ext} and R_{int} indicated that the concentrations of extrinsic oxygen vacancies and intrinsic oxygen vacancies are drastically diminished with an increase in air-annealing temperature. On the other hand, in the Raman spectra of GDC15 (*i.e.*, the same Gd content as that of GNDC5 and without Ni doping), no variations in both the F$_{2g}$ peak (at 460 cm^{-1}) and extrinsic vacancy peak (at ~560 cm^{-1}) were observed regardless of the annealing temperature (Fig. S2b†), while the intrinsic vacancy peak was attenuated with increasing annealing temperature (see Fig. S2b† inset). It has been reported that the relative amount of intrinsic oxygen vacancies in ceria is reduced due to crystallite growth upon high-temperature annealing, which is irrespective of Ni doping.[40,41] Raman analysis clearly supports that the Ni is substitutionally doped into GDC until its solubility limit when calcined at 600 °C, generating extrinsic oxygen vacancies and is subsequently exsolved upon further annealing at higher temperatures.

The microstructure evolution of NiO oxidized from Ni exsolution upon air annealing can be characterized by high-resolution transmission electron microscopy (HR-TEM). According to XRD and Raman studies, GNDC5-800 (Fig. 3a and b) could be regarded as an intermediate state between the Ni-doped and Ni fully exsolved states, whereas Ni was completely exsolved in the case of GNDC5-1250 (Fig. 3c and d). All lattice fringes were obtained by averaging ten intervals of intensity peaks in the scattering intensity plot to distinguish the difference in lattice spacing between GNDC and GDC (Fig. S3a and b†). Oxidized NiO clusters with size below 5 nm were observed in GNDC5-800 (Fig. 3b), which is indicative of partial exsolution. On the other hand, GNDC5-1250 showed NiO nanoparticles with approximately 15 nm diameter at the surface (*i.e.*, Ni was fully exsolved), as shown in Fig. 3c. This observation allows us to speculate that Ni is exsolved and oxidized to NiO clusters, subsequently protruding out as nanoparticles during the high-temperature annealing-driven grain growth, as schematically shown in Scheme 1. The remaining grains after complete exsolution of Ni exhibited a lattice spacing of 0.271 nm, which corresponded to the GDC (200) plane (Fig. 3d), which was larger than the calculated interplanar spacing of GNDC5 prior to exsolution (Fig. S1†). This value was slightly larger than that of GNDC5-800 after partial exsolution (Fig. S3a†) and indicates that GNDC5-1250 is capable of returning to Ni-undoped GDC after complete exsolution of Ni. Typically, Ni-based anodes for SOFCs are prepared from a powder mixture of NiO and GDC followed by sintering and reduction prior to use. Furthermore, we characterized the reduced GNDC5-1250 under a humidified H$_2$ atmosphere at 650 °C for 30 min by scanning transmission electron microscopy (STEM) and energy dispersive X-ray spectroscopy (EDS), as shown in Fig. 4. Ni nanoparticles reduced from NiO and attached onto the surface of GNDC5-1250 were clearly observed, whose size (~15 nm diameter) was not significantly altered during the reduction. Despite $\sim40\%$ volumetric shrinkage upon reduction of NiO to Ni,[43] the invariance in the Ni particle size indicates that thermally exsolved NiO nanoparticles are strongly attached to the surface of the GDC grains. This microstructural feature associated with Ni nanoparticles can maximize the active reaction sites, thus playing a role in yielding an ideal fuel electrode, which possesses both the high catalytic activity of the Ni nanocatalyst and the high MIEC properties of GDC upon reduction.
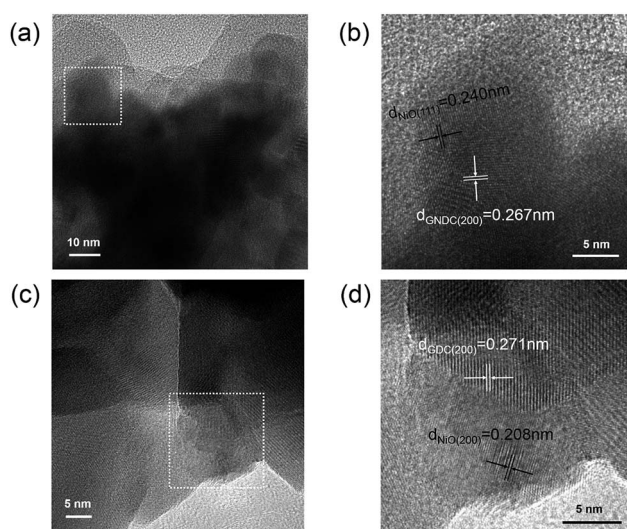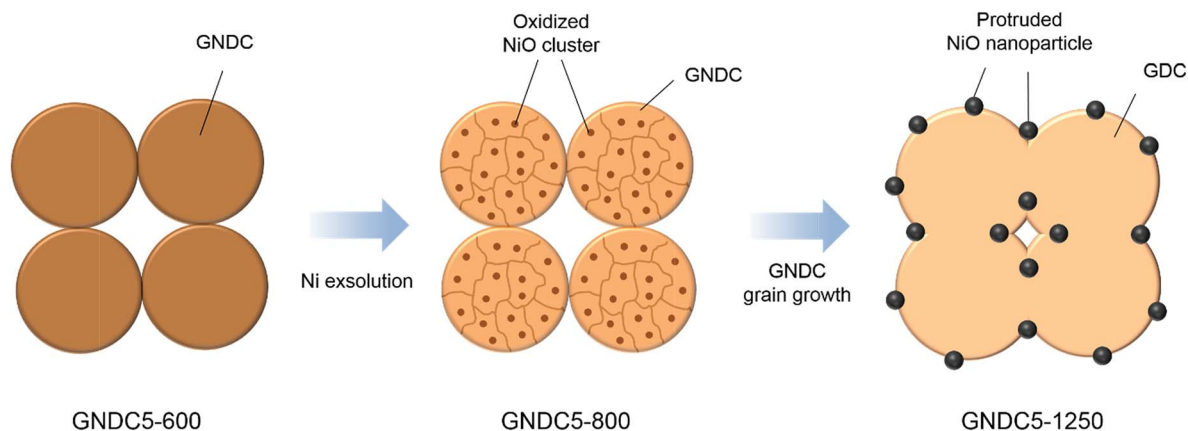
Electrochemical characterization of the GNDC electrode

To evaluate the electrochemical catalytic activity of the thermally exsolved Ni nanocatalyst after reduction with respect to bulk Ni catalyst (particle size $\sim$ 250 nm), we prepared two different symmetrical cells using pastes made of either GNDC5 powder alone or mechanically mixed NiO (particle size $\sim$ 0.3 μm) and GDC composite powder followed by sintering at 1250 °C and reduction at 650 °C. Each cell was composed of two identical electrodes with a thickness of ~20 μm deposited on both sides of the YSZ electrolyte pellet (~500 μm) (Fig. S4†). Although Pt was employed as a current collector on top of each electrode, we assumed that its catalytic contribution is negligible because it was placed out of the effective electrochemical reaction zone (ERZ, ~10 μm (ref. 21 and 50)). We performed EIS on two symmetrical cells at 650 °C under a humidified H$_2$ atmosphere (3% H$_2$O/H$_2$), as shown in Fig. 5a and b. The ohmic resistance (R_s), determined by both ion and electron conductions within the electrolyte and electrode, respectively, of the GNDC5 cell was slightly larger than that of the mechanically mixed Ni-GDC cell, possibly due to the limited volume fraction

Fig. 3 (a) HR-TEM image of GNDC5-800 regarded as an intermediate state between Ni-doped and Ni fully exsolved states and (b) its magnified image to confirm the lattice fringe. Oxidized NiO clusters with a size below 5 nm are observed. (c) HR-TEM image of GNDC5-1250 considered as a Ni fully exsolved state and (d) its magnified image. NiO nanoparticles are protruded at the surface of GDC grains. The lattice spacing of GNDC and GDC is confirmed by plotting the scattering intensities as shown in Fig. S3.†

Scheme 1 Schematic illustration of the thermal exsolution process of GNDC5. Ni is exsolved and thermally oxidized to NiO clusters, and subsequent annealing induces the growth of NiO nanoparticles protruding onto the surface of the recovered GDC phase from GNDC.
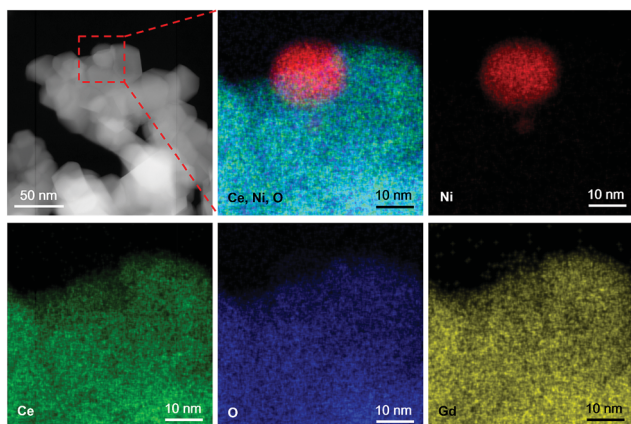

Fig. 4 HAADF image and EDS elemental maps showing the microstructure of Ni nanoparticles reduced from NiO attached onto the surface GNDC5-1250. The reduction was performed at 650 °C for 30 min.

of metallic Ni for electron conduction; however, the insignificant difference in R_s indicated that GDC retains sufficient electronic conductivity even after reduction. Interestingly, the GNDC5 electrode showed a lower R_p (1.04 Ω cm^2, one half of the arc diameter, Fig. 5a) than the mechanically mixed Ni-GDC composite electrode (R_p = 1.38 Ω cm^2, Fig. 5b) whose bulk Ni volume fraction was ~40%, despite the lower volume fraction of Ni (2%) in the thermally exsolved Ni nanocatalyst. In addition, it is substantially lower than those of other powder-processed Ni-ceria composite electrodes reported in the literature (Table S1†). For detailed analysis, the R_p was deconvoluted using a simple equivalent circuit model consisting of two serially connected resistor-capacitor models with a resistance and a constant phase element. According to a previous EIS analysis of a Ni-based composite electrode,[44,45] the first semicircle in the high-frequency range (R_{HF}) arises from the oxygen ion transport kinetics through the GDC phase and the second arc in the low-frequency region (R_{LF}) represents the electrochemical charge-transfer reaction at the TPBs (*i.e.*, Ni/GDC interface),

while the two resistances vary according to the relative contents of Ni and GDC. For example, an electrode with a high volume fraction of GDC (*i.e.*, relatively low Ni volume fraction) exhibits a small R_{HF} owing to enhanced oxygen ion transport, whereas the R_{LF} should be large due to insufficient TPB density. Thus, the composition of the Ni-GDC composite electrode is generally optimized in the range of 40–50 vol% Ni.[21] Surprisingly, the GNDC5 electrode composed of ~98 vol% GDC exhibited lower R_{HF} and R_{LF} than those of the Ni-GDC composite electrode (fitted results are shown in Table S2†), despite having only ~2 vol% of Ni. This implies that the TPB density in the GNDC5 electrode could be increased compared to the Ni-GDC composite electrode. On the other hand, the porosity of the Ni based cermet anode in SOFCs is created by burning organic additives (such as a solvent, binder and pore former) or *in situ* reduction of NiO to Ni, while insufficient porosity could impede gas phase diffusion within the electrode, possibly increasing the total R_p. Despite no NiO reduction induced pore formation in the GNDC5 electrode, their EIS responses were independent of varying total gas flow rate, demonstrating that the gas phase diffusion limit is negligible (Fig. S5†).

The cross-sectional scanning electron microscopy (SEM) image of the GNDC5 electrode after EIS measurements clearly revealed Ni nanoparticles with 10–20 nm size well-anchored on the GDC grains (Fig. 5c), whereas Ni and GDC grains were simply intermixed in the mechanically mixed Ni-GDC composite electrode (Fig. 5d). To estimate the TPB density created by the Ni nanocatalyst in the GNDC5 electrode, we measured the total perimeter of the exsolved Ni nanoparticles using ImageJ software, as shown in Fig. S6.† The TPB density from the two-dimensional image (Fig. 5c) was estimated to be ~2448 m cm^{-2}, which was ~2.5 times larger than the reported value for the mechanically mixed Ni-based composite electrode.[46] In addition, we calculated the volumetric TPB density to be ~2.4 × 10^7 m cm^{-3} assuming that the depth of the electrode in Fig. 5c was 1 μm, which was ~5.7 times larger than the reported volumetric TPB density of the Ni-YSZ composite electrode.[47] Although the porosity of the GNDC5 electrode was not considered in our estimation, the TPB density created by the Ni
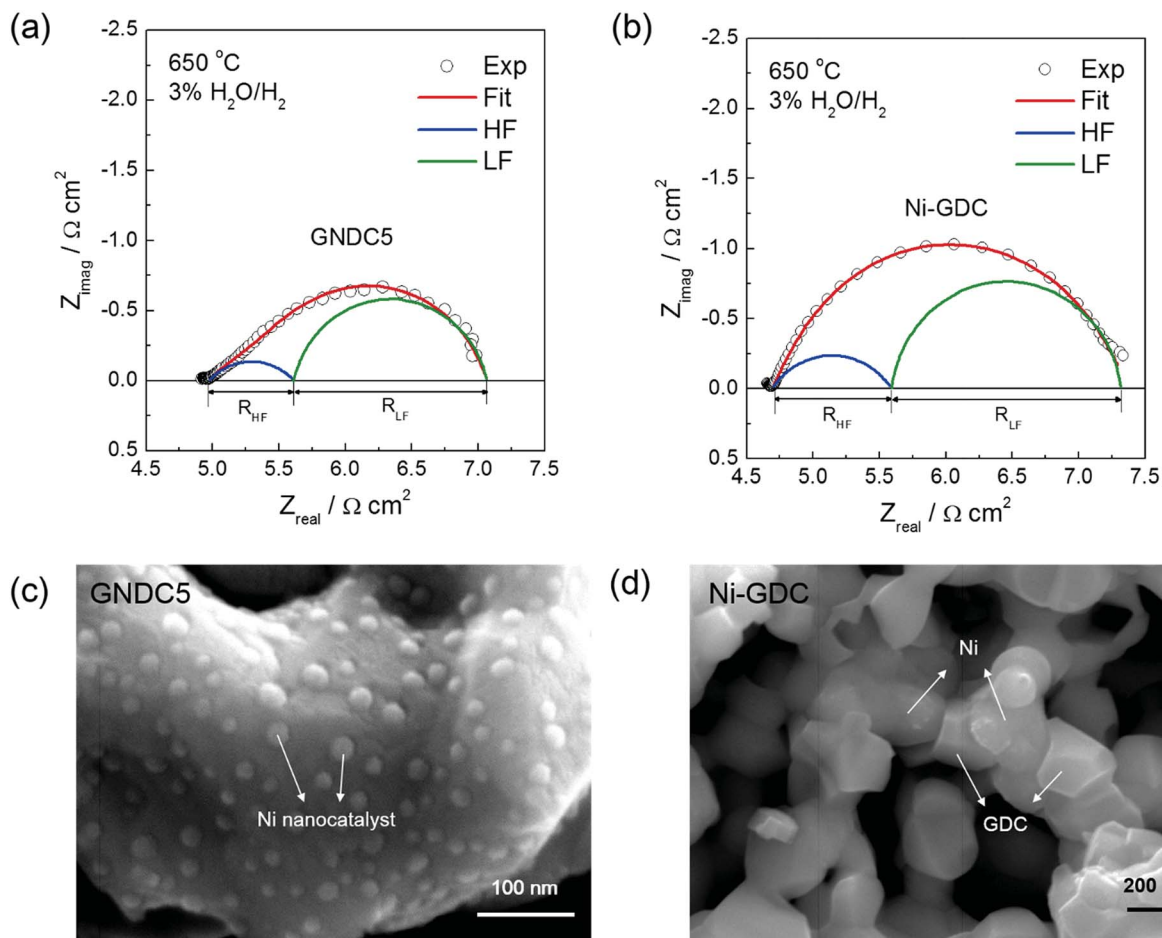
Fig. 5 Nyquist plot of the (a) synthesized GNDC5 and (b) mechanically mixed Ni–GDC composite electrodes. EIS of each symmetrical cell was measured at 650 °C in a humidified H_2 atmosphere (3% H_2O/H_2). The R_p arc was deconvoluted into two semicircles: R_{HF} represents the resistance for oxygen ion transport through the GDC phase (blue), whereas R_{LF} corresponds to the electrochemical charge-transfer reaction resistance (green). Cross-sectional SEM image of the (c) GNDC5 electrode showing the Ni nanocatalyst anchored onto the GDC surface, and (d) Ni–GDC composite electrode revealing simply intermixed Ni and GDC grains. Both images are obtained after EIS measurements.

nanocatalyst should be still large as compared to that of the mechanically mixed Ni–GDC composite electrode, for example, ~3.4 times larger TPB density considering ~40 vol% porosity. This was in agreement with the smaller R_{LF} of GNDC5 as compared with that of the Ni–GDC composite electrode obtained from the EIS results. The activation energy (E_a) for these electrodes was obtained from the EIS measurements in the range of 650–500 °C. The calculated E_a values from the Arrhenius relation (i.e., linear dependence in a plot of $\ln(1/R_p)$ over $1/T$) of the GNDC5 electrode and mechanically mixed Ni–GDC composite electrode were 1.06 eV and 1.23 eV, respectively (Fig. S7†). According to a previous study on the electrode process for the hydrogen evolution reaction, the main elementary reaction step can be distinguished into three distinct steps based on the calculated E_a: a gas phase diffusion step when E_a < 0.2 eV, hydrogen adsorption/dissociation step when E_a ~ 0.4–0.5 eV, and electrochemical charge-transfer reaction when E_a ~ 0.8–1.2 eV.[48] While both electrode reactions are identically rate-determined by a charge-transfer reaction at TPBs, the R_p of the GNDC5 electrode was further lowered with respect to the

mechanically mixed Ni–GDC electrode with decreasing temperature, suggesting that the Ni nanocatalyst thermally exsolved from GNDC can play an effective role especially at lower temperatures.

To support the catalytic role of the exsolved Ni nanocatalyst in the GNDC5 electrode, we further conducted EIS measurements on GDC20 (i.e., synthesized powder without Ni doping)-based symmetrical cells (sintered at 1250 °C and reduced at 650 °C). As shown in Fig. S8,† the R_p of the GDC20 electrode became significantly larger than that of the GNDC5 electrode, while it could be expected that the resistance associated with the charge-transfer reaction particularly increased. This implies that the electrochemical reaction is suppressed because TPB cannot exist without the exsolved Ni catalyst. To evaluate the structural stability toward thermal and electrochemical stresses, accelerated lifetime tests (ALTs)[49] were performed on the GNDC5 electrode at 650 °C by applying a pyramid-type cyclic current load in the range of 0–1 A cm^{-2}. Each current load lasted 30 min (histogram), and subsequently, EIS was performed to obtain the R_p (line plot with a triangle marker), as

shown in Fig. 6. The R_p of the GNDC5 electrode remained nearly constant while the current cycles were applied up to 50 h, indicating that the TPB density induced by the Ni nanocatalyst was thermally and electrochemically stable. Therefore, it can be explained that the unique anchored structure of the Ni nano-catalyst onto the GDC prevents further agglomeration under severe operation conditions.

Full cell performances

The SOFC is one of the most promising energy conversion devices, in which electrical energy can be generated by supplying fuel and oxidants.[50] The state-of-the-art SOFC design is an anode-supported configuration with a thin electrolyte (10–20 μm), and the most common and simplest anode reaction is $H_2 + O^{2-} \leftrightarrow H_2O + 2e^-$, which can be easily catalyzed using a Ni-GDC composite anode. Typically, an anode functional layer (AFL) comprising submicron-sized Ni and GDC particles is introduced at the interface between an anode support and the electrolyte to maximize the TPB density, where the effective ERZ is ~10 μm.[21,51] Because it was confirmed that the thermally exsolved Ni nanocatalyst from GNDC5 could effectively enhance the TPB density, we introduced GNDC5 (thickness ~ 5 μm; thickness dependence will be discussed below) as an AFL and compared it with a submicron-sized bulk Ni-GDC composite AFL (thickness ~ 10 μm). For precise comparison, an identical anode-supported cell structure except for the AFL thickness was fabricated, as shown in Fig. 7a (i.e., Ni-GDC|AFL(Ni-GDC or GNDC5)|GDC|LSCF-GDC, each cell is denoted as the Ni-GDC cell and GNDC5 cell). The current–voltage (I–V) characteristics and the corresponding power densities of the Ni-GDC cell and GNDC5 cell at different temperatures (650–550 °C) are shown in Fig. 7b. The backscattering electron mode of SEM confirmed that both the cells exhibited similar microstructures of the cathode and electrolyte with different AFL thicknesses (Fig. S9†). Additionally, both the cells showed almost identical open circuit voltages at each temperature and similar perfor-mances at 650 °C. However, the difference in power density arose at a lower temperature, with the GNDC5 cell

outperforming the Ni-GDC cell. At 0.7 V, the Ni-GDC cell exhibited current densities of 0.41 A cm^{-2} and 0.15 A cm^{-2} at 600 °C and 550 °C, respectively, whereas the GNDC5 cell showed current densities of 0.49 A cm^{-2} (~120% increase with respect to the Ni-GDC cell) and 0.20 A cm^{-2} (~133%) at 600 °C and 550 °C, respectively. It should be noted that the performance level of our Ni-GDC control cell matches well with the values reported by previous studies for the Ni-GDC AFL system.[21,51] The EIS measurements at 650–550 °C for both the cells are summarized in Table S3.† At 650 °C, the total electrode R_p of the full cell under OCV conditions was only 0.103 Ω cm^2, which was even lower than that of the GNDC5 electrode obtained from the symmetrical cell (1.04 Ω cm^2) under a reducing atmosphere. It is speculated that the electrochemical reac-tions at both the cathode and anode are promoted under an oxygen partial pressure gradient across the full cell. At the OCV state of the full cell, the concentration gradient of O^{2-} across the electrolyte is generated owing to different oxygen partial pressures between the cathode and anode, in which this gradient can enhance the reaction kinetics of each electro-chemical reaction. On the other hand, this concentration gradient of O^{2-} in the symmetrical cell is zero under OCV conditions; thus no additional driving force exists for the anodic reaction, in turn increasing the R_p. Although the total R_p of the full cell includes both cathodic and anodic effects, which are hardly distinguished from the EIS response, the GNDC5 cell consistently revealed a larger R_s and smaller R_p as compared to those of the Ni-GDC cell at all temperatures (Table S3†). In addition, the difference in R_p increased with decreasing temperature (Fig. 7c), similar to the cell perfor-mance variation in Fig. 7b and Arrhenius relation in Fig. S7.† While the power density in the high-current region was influenced by complicated contributions of activation, ohmic, and concentration polarizations, the activation polarization associated with TPB density reduced when the Ni nanocatalyst in the GNDC5 AFL was used at lower temperatures (<650 °C), assuming identical cathodic polarization. Although this is not such a large improvement, it should be noted that sufficient TPB density of the anode can be obtained with only ~2 vol% of Ni using thermal exsolution from GNDC5.

To further improve the cell performance, the thickness of the GNDC5 AFL needs to be optimized because an effective ERZ is considered as ~10 μm from the electrolyte.[44] We fabricated two different cells with ~5 μm (cell-A, Fig. S10a†) and ~11 μm (cell-B, Fig. S10b†) GNDC5 AFL thicknesses, with ~20 μm-thick electrolyte. Interestingly, cell-B exhibited lower I–V perfor-mance despite having a thicker GNDC5 AFL (Fig. S10c†) while the R_p was almost identical (Fig. S10d†). It can be speculated that the effective ERZ for GNDC5 was within ~5 μm because the R_p of cell-A (AFL ~ 5 μm) and cell-B (AFL ~ 11 μm) were almost identical, while the sluggish electronic conduction through the GNDC5 layer (>5 μm) due to insufficient Ni volume could directly impede the cell performance by increasing the R_s. According to these observations, it is clear that the thermally exsolved Ni nanocatalyst enhances the electrochemical charge-transfer reaction due to the increased TPB density; however, ohmic polarization should be minimized to achieve high-
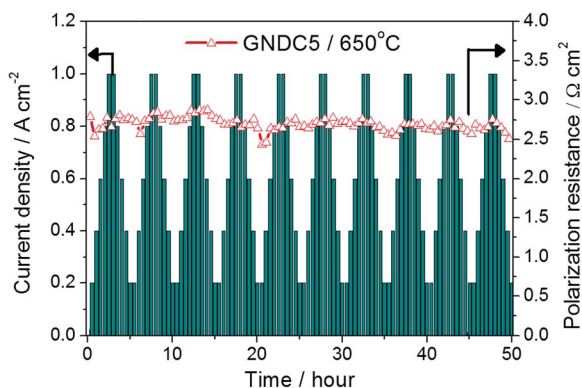

Fig. 6 Polarization resistance (R_p) of the GNDC5 electrode during the ALT at 650 °C. The histogram shows the applied current load over 30 min and the line plot with the triangle marker shows R_p variation measured after each current load.

This journal is © The Royal Society of Chemistry 2018

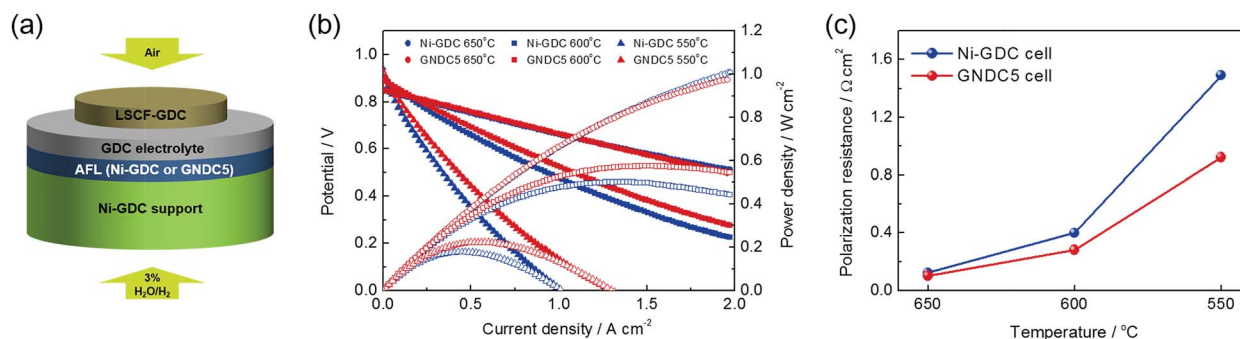*J. Mater. Chem. A*, 2018, **6**, 18133–18142 | **18139**

Fig. 7 (a) Schematic illustration of the anode-supported SOFC structure with two different AFLs (Ni-GDC composite or GNDC5). (b) Current−voltage characteristics of the GNDC5 cell (red) and Ni-GDC cell (blue) at different temperatures. 3% H_2O/H_2 and air are supplied to the anode and cathode, respectively. (c) The corresponding R_p measured at 650, 600, and 550 °C.
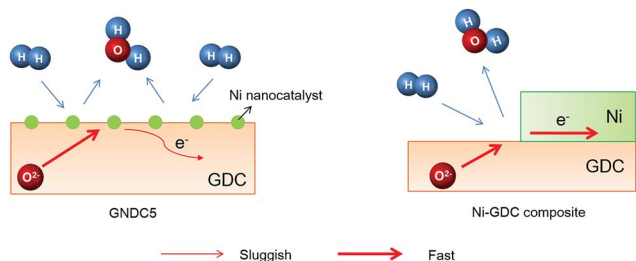
Scheme 2 Schematic illustration of the SOFC anode reaction on the Ni nanocatalyst-exsolved GNDC5 electrode and mechanically mixed Ni-GDC composite electrode. The charge-transfer reaction is enhanced owing to increased TPB density endowed by Ni nanocatalysts in the GNDC5 electrode, but sluggish electron conduction through GDC could increase the total ohmic polarization.

performance SOFCs because of the sluggish electronic conduction through the GNDC5 layer (i.e., recovered GDC from GNDC), as illustrated in Scheme 2.

Conclusions

In summary, we, for the first time, demonstrated a facile Ni exsolution from GNDC through an in-depth understanding of the thermal behavior of exsolved Ni and the GDC host oxide. Upto 5 mol% Ni can be substitutionally doped into GDC forming GNDC5, from which Ni was thermally exsolved and oxidized into NiO clusters with 5 nm size, which subsequently protruded out as nanoparticles (∼15 nm) during the high-temperature annealing-driven grain growth of GNDC. Therefore, Ni was strongly attached to GDC, yielding a surface-anchored nanocatalyst after reduction. Although the R_s of the GNDC5 electrode inevitably increased due to the limited volume fraction of metallic Ni, the R_p decreased compared with that of the mechanically mixed Ni-GDC composite electrode, owing to the significantly increased TPB density provided by the Ni nanocatalyst. In addition, our thermally driven Ni-exsolved GNDC5 revealed great potential as an AFL for SOFCs, improving the electrochemical performance particularly at lower temperatures.

Experimental section

Synthesis and analyses of GNDC/GDC powders

GNDC powders were prepared by a Pechini-type polymerizable complex method. Required amounts of metal nitrate precursors, $Ni(NO_3)_2 \cdot 6H_2O$ (Junsei Chemical Co., 97.0%), $Gd(NO_3)_3 \cdot 6H_2O$ (Sigma Aldrich, 99.9%), and $Ce(NO_3)_3 \cdot 6H_2O$ (Sigma Aldrich, 99.9%), were dissolved in DI water with ethylene diamine tetra-acetic acid (EDTA, Ducksan Pure Chemical 99%) as a chelating agent and heated to 65 °C. The solution pH was adjusted to 6 using ammonium hydroxide, and subsequently, ethylene glycol (Sigma Aldrich, 99.5%) was added to this solution as a polymerization agent at 95 °C. The blue polymeric solution (should be colorless without the Ni precursor for synthesis of GDC) was gradually condensed up to 300 °C, which induced self-ignition of the polymer complex and yielded ash-colored intermediates.[52,53] Finally, GNDC powders were obtained after calcination at 600 °C for 4 h. Similarly, GDC powders (i.e., GDC15 and GDC20) were synthesized without a Ni precursor. For further analyses of GNDC5, the calcined powder was annealed at 800 °C and 1250 °C, respectively, for 3 h. The phase formation of the synthesized powders was examined using a Rigaku Miniflex 600 X-ray diffractometer (Cu K_α, scan rate = 1° min^{-1}). In all XRD measurements, α-Al_2O_3 powders (JCPDS 46-1212, circular symbol in Fig. 1a) were employed as an internal reference for the calibration of peak positions and intensities of GNDCs and GDC.[54] For unit cell parameter calculations, quantitative analyses by the reference intensity ratio method were performed using PDXL (Rigaku Corporation, Japan) software. Raman scattering analysis was performed at room temperature under ambient conditions using a Horiba Jovin Yvon LabRam Aramis spectrometer equipped with a CCD camera. An Ar-ion laser (514 nm) was used as the excitation source, with a beam intensity of ∼1.0 mW, measured at the sample surface, to avoid heating. The instrument was calibrated with a silicon wafer using the 521 cm^{-1} peak. Each Raman spectrum was normalized by the F_{2g} peak intensity, and a Lorentzian function was employed to deconvolute the non-degenerate mode. The microstructures of GNDC5 powders and the corresponding high-angle annular dark field (HAADF) images and STEM-EDS maps were obtained (Talos F200X, FEI,

Hillsboro, OR, USA) at 200 kV acceleration voltage. For precise comparison, the scattering intensities of lattice fringes were obtained using Gatan software.

Fabrication and characterization of symmetrical cells

To evaluate the electrocatalytic activities, we fabricated an electrolyte-supported symmetrical half-cell as follows. For the electrolyte support, commercial YSZ powders (8 mol% Y_2O_3–ZrO_2, TZ-8Y, Tosoh Co., Japan) were pressed into a pellet with a diameter of 25 mm, sintered at 1500 °C for 5 h in air, and subsequently polished to 0.5 mm thickness. The synthesized GNDC powders as well as the mechanically mixed NiO (J.T. Bakers) and GDC10 (Fuel Cell Materials) powders (5 : 5 in a weight ratio) were used to prepare the screen printing paste, respectively, which is a mixture of the powder and an organic solvent composed of ethyl cellulose and α-terpineol (Sigma Aldrich). A circular electrode with 1 cm^2 area was obtained at the center of the YSZ electrolyte pellet at each side by screen printing through a 300-size mesh and was subsequently sintered at 1250 °C for 3 h in air to attain a porous microstructure with ~20 μm thickness. A Pt mesh and Pt paste (5542, ESL Electroscience, PA, USA) were employed as current collectors. Electrochemical impedance spectra were obtained at various temperatures (500–650 °C) using a Solartron SI 1260/1287 instrument in the frequency range of 100 kHz to 0.01 Hz with an AC amplitude of 20 mV. Humidified hydrogen (3% H_2O/H_2) was equally supplied to both sides of the symmetrical cells during characterization. A field emission SEM (JSM-7800F, JEOL, Japan) was employed to confirm the microstructure of each electrode after EIS measurements. To estimate the TPB density, ImageJ software (National Institute of Health) was used to measure the total perimeter of the exsolved Ni nanoparticles. A pyramid-type cyclic current load was supplied for the ALT, and each cyclic load consisted of an increasing step current from 0 to 1 A cm^{-2} and then a returning step current from 1 to 0 A cm^{-2} with 0.2/−0.2 A cm^{-2}. At each step, a constant current density (*i.e.*, galvanostatic) was applied for 30 min, and subsequently, EIS was measured.

Full cell fabrication and characterization

For the Ni-GDC support, commercial NiO (J.T. Bakers) and GDC10 (Fuel Cell Materials) powders (6 : 4 in a weight ratio) were mixed with 10 wt% of carbon black as a pore former in ethanol solvent and ball-milled for 24 h. After drying and sieving, the powder mixture was pressed into a pellet with a diameter of 25 mm and burned at 1200 °C for 3 h. For all dip-coating processes, we used isopropyl alcohol and toluene (2 : 1 vol%), DISPERBYK-2163 (BYK Additives & Instruments) and polyvinyl butyral (Sigma Aldrich) as a solvent, dispersant, and binder, respectively, for the slurry mixture. For the Ni-GDC cell, submicron-sized NiO and GDC powders (Fuel Cell Materials, 5 : 5 in a weight ratio, 2.5 vol% of solid loading) were first dip-coated onto the Ni-GDC support to deposit the Ni-GDC composite AFL and pre-sintered at 1150 °C for 3 h. Subsequently, GDC electrolyte (3 vol% of solid loading, ~13 μm) was dip-coated and co-sintered at 1350 °C for 3 h. The LSCF-GDC

(Fuel Cell Materials; 5 : 5, w/w) composite cathode was screen-printed at the unpolished side of the electrolyte and sintered at 1000 °C for 4 h. After sintering of the cathode, the Pt mesh attached with Pt paste and Ni felts were employed as current collectors for the cathode and anode, respectively. For the GNDC5 cell, all the processes were identical except for the AFL; the composite AFL was replaced with the GNDC5 AFL. For the GNDC5 AFL dip-coating slurry, the as-synthesized GNDC5 powder (2.2 vol% of solid loading) and a sufficient amount of binder were dissolved in order to ensure the porosity of the AFL after sintering (pre-sintered at 1150 °C for 3 h). To adjust the thickness of the AFL, the solid loading of GNDC5 powder was varied (2.2 vol% for cell-A and 2.5 vol% for cell-B), while the GDC electrolyte (3.5 vol% of solid loading, ~20 μm) and all other conditions were fixed. For electrochemical measurements, *I–V* curves and EIS spectra were measured while supplying 80 sccm of 3% H_2O/H_2 to the anode and 400 sccm of ambient air to the cathode.

Conflicts of interest

There are no conflicts to declare.

Acknowledgements

References

1 J. T. S. Irvine, D. Neagu, M. C. Verbraeken, C. Chatzichristodoulou, C. Graves and M. B. Mogensen, *Nat. Energy*, 2016, **1**, 15014.

2 Y. Zhu, W. Zhou, R. Ran, Y. Chen, Z. Shao and M. Liu, *Nano Lett.*, 2016, **16**, 512–518.

3 H. Wei, K. Xie, J. Zhang, Y. Zhang, Y. Wang, Y. Qin, J. Cui, J. Yan and Y. Wu, *Sci. Rep.*, 2014, **4**, 5156.

4 Y.-F. Sun, Y.-Q. Zhang, J. Chen, J.-H. Li, Y.-T. Zhu, Y.-M. Zeng, B. S. Amirkhiz, J. Li, B. Hua and J.-L. Luo, *Nano Lett.*, 2016, **16**, 5303–5309.

5 Z. Du, H. Zhao, S. Yi, Q. Xia, Y. Gong, Y. Zhang, X. Cheng, Y. Li, L. Gu and K. Świerczek, *ACS Nano*, 2016, **10**, 8660–8669.

6 J. Myung, D. Neagu, D. N. Miller and J. T. S. Irvine, *Nature*, 2016, **537**, 528–531.

7 O. Kwon, S. Sengodan, K. Kim, G. Kim, H. Y. Jeong, J. Shin, Y.-W. Ju, J. W. Han and G. Kim, *Nat. Commun.*, 2017, **8**, 15967.

8 D. S. Tsvetkov, I. L. Ivanov, D. A. Malyshkin and A. Y. Zuev, *J. Mater. Chem. A*, 2016, **4**, 1962–1969.

9 D. E. Fowler, A. C. Messner, E. C. Miller, B. W. Slone, S. A. Barnett and K. R. Poeppelmeier, *Chem. Mater.*, 2015, **27**, 3683–3693.

This journal is © The Royal Society of Chemistry 2018

J. Mater. Chem. A, 2018, **6**, 18133–18142 | 18141

10 T. Zhu, H. E. Troiani, L. V. Mogni, M. Han and S. A. Barnett, *Joule*, 2018, **2**, 478–496.

11 R. Glaser, T. Zhu, H. Troiani, A. Caneiro, L. Mogni and S. Barnett, *J. Mater. Chem. A*, 2018, **6**, 5193–5201.

12 D. Neagu, G. Tsekouras, D. N. Miller, H. Ménard and J. T. S. Irvine, *Nat. Chem.*, 2013, **5**, 916–923.

13 D. Neagu, T.-S. Oh, D. N. Miller, H. Ménard, S. M. Bukhari, S. R. Gamble, R. J. Gorte, J. M. Vohs and J. T. S. Irvine, *Nat. Commun.*, 2015, **6**, 8120.

14 T.-S. Oh, E. K. Rahani, D. Neagu, J. T. S. Irvine, V. B. Shenoy, R. J. Gorte and J. M. Vohs, *J. Phys. Chem. Lett.*, 2015, **6**, 5106–5110.

15 G. Xiao, S. Wang, Y. Lin, Y. Zhang, K. An and F. Chen, *ACS Appl. Mater. Interfaces*, 2014, **6**, 19990–19996.

16 G. C. Kostogloudis, G. Tsiniarakis and C. Ftikos, *Solid State Ionics*, 2000, **135**, 529–535.

17 M. Mogensen and S. Skaarup, *Solid State Ionics*, 1996, **86–88**(part 2), 1151–1160.

18 K. T. Lee, N. J. Vito and E. D. Wachsman, *J. Power Sources*, 2013, **228**, 220–228.

19 J. B. Goodenough and Y.-H. Huang, *J. Power Sources*, 2007, **173**, 1–10.

20 J. R. Wilson and S. A. Barnett, *Electrochem. Solid-State Lett.*, 2008, **11**, B181–B185.

21 K. T. Lee, N. J. Vito, H. S. Yoon and E. D. Wachsman, *J. Electrochem. Soc.*, 2012, **159**, F187–F193.

22 D. Papargyriou and J. T. S. Irvine, *Solid State Ionics*, 2016, **288**, 120–123.

23 B. H. Park and G. M. Choi, *Solid State Ionics*, 2014, **262**, 345–348.

24 S. Boulfrad, M. Cassidy and J. T. S. Irvine, *Solid State Ionics*, 2011, **197**, 37–41.

25 A. J. Jacobson, *Chem. Mater.*, 2010, **22**, 660–674.

26 M. Mogensen, N. M. Sammes and G. A. Tompsett, *Solid State Ionics*, 2000, **129**, 63–94.

27 M. Mogensen, T. Lindegaard, U. R. Hansen and G. Mogensen, *J. Electrochem. Soc.*, 1994, **141**, 2122–2128.

28 F. Pilger, A. Testino, A. Carino, C. Proff, A. Kambolis, A. Cervellino and C. Ludwig, *ACS Catal.*, 2016, **6**, 3688–3699.

29 W. Qi, K. Xie, M. Liu, G. Wu, Y. Wang, Y. Zhang and Y. Wu, *RSC Adv.*, 2014, **4**, 40494–40504.

30 J. Myung, T. H. Shin, X. Huang, G. Carins and J. T. S. Irvine, *Int. J. Hydrogen Energy*, 2015, **40**, 12003–12008.

31 A. Thurber, K. M. Reddy, V. Shutthanandan, M. H. Engelhard, C. Wang, J. Hays and A. Punnoose, *Phys. Rev. B*, 2007, **76**, 165206.

32 X. Wang, M. Shen, J. Wang and S. Fabris, *J. Phys. Chem. C*, 2010, **114**, 10221–10228.

33 C. R. Hubbard and R. L. Snyder, *Powder Diffr.*, 1988, **3**, 74–77.

34 D.-J. Kim, *J. Am. Ceram. Soc.*, 1989, **72**, 1415–1421.

35 S. J. Hong and A. V. Virkar, *J. Am. Ceram. Soc.*, 1995, **78**, 433–439.

36 S. W. Oh, H. J. Bang, Y. C. Bae and Y.-K. Sun, *J. Power Sources*, 2007, **173**, 502–509.

37 L. Barrio, A. Kubacka, G. Zhou, M. Estrella, A. Martínez-Arias, J. C. Hanson, M. Fernández-García and J. A. Rodriguez, *J. Phys. Chem. C*, 2010, **114**, 12689–12697.

38 S.-Y. Chen, R.-J. Chen, W. Lee, C.-L. Dong and A. Gloter, *Phys. Chem. Chem. Phys.*, 2014, **16**, 3274.

39 P. Sathishkumar, R. V. Mangalaraja, T. Pandiyarajan, M. A. Gracia-Pinilla, N. Escalona, C. Herrera and R. Garcia, *RSC Adv.*, 2015, **5**, 22578–22586.

40 J. E. Spanier, R. D. Robinson, F. Zhang, S.-W. Chan and I. P. Herman, *Phys. Rev. B*, 2001, **64**, 245407.

41 Z. V. Popović, Z. Dohčević-Mitrović, M. Šćepanović, M. Grujić-Brojčin and S. Aškrabić, *Ann. Phys.*, 2011, **523**, 62–74.

42 D. Devaiah, G. Thrimurthulu, P. G. Smirniotis and B. M. Reddy, *RSC Adv.*, 2016, **6**, 44826–44837.

43 Y. Brodnikovskyi, B. Vasyliv, V. Podhurska, M. Andrzejczuk, N. McDonald, O. Kyrpa, O. Ostash, R. Steinberger-Wilckens and M. Lewandowska, *J. Electrochem. Sci. Eng.*, 2016, **6**, 113–121.

44 S. Primdahl and M. Mogensen, *Solid State Ionics*, 2002, **152–153**, 597–608.

45 S. Primdahl and M. Mogensen, *J. Electrochem. Soc.*, 1997, **144**, 3409–3419.

46 M. Brown, S. Primdahl and M. Mogensen, *J. Electrochem. Soc.*, 2000, **147**, 475–485.

47 J. R. Wilson, W. Kobsiriphat, R. Mendoza, H.-Y. Chen, J. M. Hiller, D. J. Miller, K. Thornton, P. W. Voorhees, S. B. Adler and S. A. Barnett, *Nat. Mater.*, 2006, **5**, 541–544.

48 T. Ishihara and H. Zhong, *Scr. Mater.*, 2011, **54**, 108–111.

49 H. S. Song, S. Lee, D. Lee, H. Kim, S. H. Hyun, J. Kim and J. Moon, *J. Power Sources*, 2010, **195**, 2628–2632.

50 T. Ishihara, *J. Korean Ceram. Soc.*, 2016, **53**, 469–477.

51 K. T. Lee, H. S. Yoon, J. S. Ahn and E. D. Wachsman, *J. Mater. Chem.*, 2012, **22**, 17113–17120.

52 V. Agarwal and M. Liu, *J. Mater. Sci.*, 1997, **32**, 619–625.

53 S. Li, Z. Lü, B. Wei, X. Huang, J. Miao, G. Cao, R. Zhu and W. Su, *J. Alloys Compd.*, 2006, **426**, 408–414.

54 M. A. Wandt and A. L. Rodgers, *Clin. Chem.*, 1988, **34**, 289–293.